IJMGE
Int. J. Min.& Geo-Eng.
Vol.47, No.2, Dec. 2013, pp. 163-179

Three-Dimensional Geostatistical Analysis of Rock Fracture Roughness and Its Degradation with Shearing

Nima Babanouri*, Saeed Karimi Nasab

Department of Mining Engineering, Shahid Bahonar University of Kerman, Kerman, Iran

Received 5 November 2013; Received in revised form 3 December 2013; accepted 20 December 2013
Corresponding author*: bbn.nima@gmail.com*

Abstract
Three-dimensional surface geometry of rock discontinuities and its evolution with shearing are of great importance in understanding the deformability and hydro-mechanical behavior of rock masses. In the present research, surfaces of three natural rock fractures were digitized and studied before and after the direct shear test. The variography analysis of the surfaces indicated a strong non-linear trend in the data. Therefore, the spatial variability of rock fracture surfaces was decomposed to one deterministic component characterized by a base polynomial function, and one stochastic component described by the variogram of residuals. By using an image-processing technique, 343 damaged zones with different sizes, shapes, initial roughness characteristics, local stress fields, and asperity strength values were spatially located and clustered. In order to characterize the overall spatial structure of the degraded zones, the concept of 'pseudo-zonal variogram' was introduced. The results showed that the spatial continuity at the damage locations increased due to asperity degradation. The increase in the variogram range was anisotropic and tended to be higher in the shear direction; thus, the direction of maximum continuity rotated towards the shear direction. Finally, the regression-kriging method was used to reconstruct the morphology of the intact surfaces and degraded areas. The cross-validation error of interpolation for the damaged zones was found smaller than that obtained for the intact surface.

Keywords: *Rock fracture roughness, Spatial structure, Variography, Degraded zones, Regression-kriging, Image processing*

1. Introduction

Small changes in properties of rock fractures may lead to significant changes in the safety factor of rock structures such as surface and underground excavations, dam foundations, and geothermal reservoirs. Of parameters influencing, the morphology of rock fracture surface is of particular importance in studying the mechanical and hydraulic behavior of rock masses. Therefore, many methods have been proposed to characterize the roughness of rock discontinuities. Most of the available methods have summarized the surface roughness in terms of empirical parameters, such as joint roughness coefficient (JRC) [1], statistical parameters, such as the root mean square of first derivatives (Z_2) [2], or fractal parameters, such as fractal dimension (D) [3,4], which have been usually calculated for two-dimensional profiles along the fracture surface. However, rock fracture morphology could be studied using a comprehensive three-dimensional modeling of the surface geometry [5-7]. To this end, some attempts have been made to describe the roughness of rock discontinuities and reconstruct their topography using geostatistical tools [5,6]. Results show that the application of kriging could reasonably increase the resolution of the measured topography of rock fractures and fill the gaps in the point cloud. Variogram, which forms the basis of geostatistics, describes the

spatial variability and provides a description of the surface structure in any direction.

The roughness of a fracture surface can be generally characterized by two components: a large-scale undulation, or waviness, and small-scale roughness, or unevenness [8]. The waviness controls the initial direction of shear displacement relative to the mean discontinuity plane, while the unevenness plays an important role in mobilizing the shear strength. Therefore, these two aspects of rock fracture roughness should be distinguished in studying and describing the spatial structure of rock fracture surfaces.

Asperity degradation leads to the evolution of the spatial structure of rock fracture surfaces and formation of damage areas during shearing. Ladanyi and Archambault proposed the ratio of the degraded asperities area, a_s, for quantifying the degree of surface evolution and presented a relationship for estimating this parameter [9]. The main drawback of this model is that the initial roughness effect is ignored in estimating the damaged area. Kwafniewski and Wang developed a relationship for predicting the changes of fractal dimension of 2D profiles of the rock fracture surface with shearing as functions of the plastic work [10]. Asadi et al. simulated the asperity degradation of synthetic and natural rock fracture profiles during the direct shear test using a two-dimensional bonded particle model [11]. Homand et al. proposed a degradation model based on 3D measurements of fracture surfaces before and after shearing [12]. Using image-processing tools, Gentier et al. were able to investigate the dependence of size and location of damaged areas on the local geometry of the fracture surface [13]. Grasselli supposed that only the asperities steeped against the shear direction with an apparent dip greater than a threshold value involved in mobilization of the shear strength [7,14]. The spatial distribution of damaged zones predicted by the Grasselli's model showed a close agreement with the experimental results obtained from direct shear tests. He argued that this phenomenon can only be understood by studying the full 3D geometry of the fracture surface instead of considering a number of individual profiles [7,14].

The objective of this research is to compare the spatial structure in intact and degraded areas of rock fracture surfaces. To do end, the morphology of plaster replicas of three natural rock fractures with different roughness characteristics was considered before and after the shear test. The topography of surfaces was measured using the advanced topometric sensor technique at a high data density and precision. In addition to different surface geometries, the plaster fractures had different strength properties and were subjected to shear stress under different levels of the constant normal load. The damaged areas were identified and clustered by image-processing analyses of the sheared surface image. Finally, we evaluated the efficiency of the regression-kriging method in reconstructing the topography of the intact surfaces and degraded areas using a cross-validation procedure.

2. Topography data

In this research, the surface topography of three natural rock fractures was studied before/after shearing. The natural rock fractures, taken from the Gol-e-Gohar iron ore mine (Iran), had surfaces of high, medium, and low roughness that are respectively referred to as S1, S2, and S3 hereafter. Silicon molds of the parent rock fractures were first prepared and then cylindrical plaster replicas with the diameter of 60 mm were constructed [15]. Since the fracture replicas were produced with different ratios of plaster to water (P/W), they had different strength values. Surfaces of the plaster replicas were painted red so that even small degree of damage during the shearing process could be easily detected.

The morphology of the surfaces was scanned using an advanced topometric sensor (ATS) system. ATS systems provide an optical method based on a combination of white light fringe projection, triangulation, and phase shifting for fast and accurate calculation of high-dense 3D point clouds [7,14,16]. The resolution of the collected topography data was 0.05 mm in x- and y-directions with an elevation (z) measurement accuracy of up to 2 μm. Figure 1 shows the triangulated surfaces obtained from the 3D measurements along with the corresponding estimated *JRC* values.

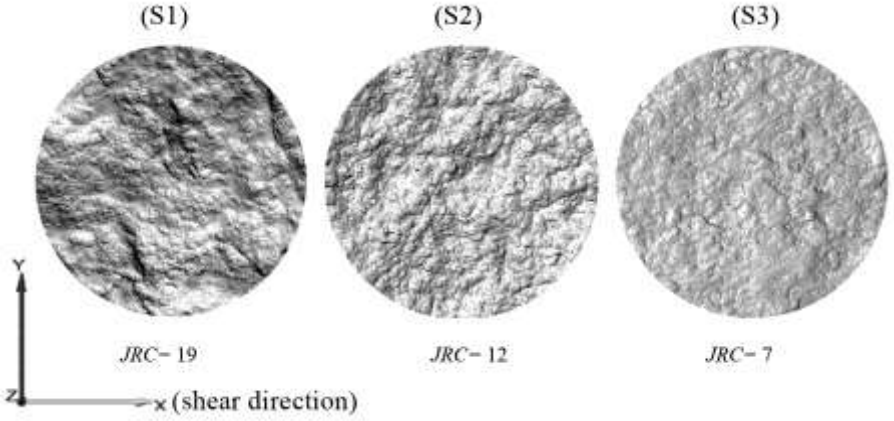

Figure 1. Triangulated surfaces obtained from 3D measurements.

The fracture replicas were subjected to direct shear tests with different values of normal stress. Each test was conducted under constant normal load (CNL) condition and ended after a shear displacement of 8 mm [15]. Table 1 represents values of the parameters *P*/*W*, *JRC*, uniaxial compressive strength (σ_c) of the fracture wall, and applied normal stress (σ_n). After cleaning the sheared surfaces from gouge material created during the shearing, they were scanned for a second time.

Table 1. Characteristics of the plaster replicas and conducted direct shear tests [15].

Surface	*P/W*	*JRC*	σ_c (MPa)	σ_n (MPa)
S1	4	19	52.12±2.14	1.30
S2	3	12	41.59±1.18	2.00
S3	2	7	17.24±3.78	0.57

3. Initial spatial structure of rock fractures

3.1. Geostatistics in brief

The first step in geostatistical analysis is to identify the spatial structure of a regionalized variable (here the elevation of the surface points) . Continuity and variability of fracture surfaces were described using the variogram (originally named semivariogram). The value of variogram (γ) for the lag vector of *h* is defined as follows [17]:

$$\gamma(h)=\frac{1}{2N(h)}\sum_{1}^{N(h)}[z(X+h)-z(X)]^2 \quad (1)$$

where *z* is the elevation; *X* is the vector of spatial coordinates (*X* =(*x,y*) in this case); *N(h)* is the number of pairs of points separated by *h*. A plot of γ(*h*) versus *h* is known as the variogram. A variogram is isotropic if its value depends only on the magnitude of *h;* it can be considered anisotropic when the direction of *h* influences the value of the variogram as well. Theoretically, when *h* approaches zero, the value of the variogram must be minimized to zero, but variograms usually do not comply with such conditions in reality. The value of the variogram at the origin is called the nugget effect (C_0), indicating the amount of the non-spatial noise whose typical source is the measurement error. Beyond a certain lag distance, known as the range (*a*), the values of the regionalized variable are uncorrelated, and the variogram does not change significantly. A wide range indicates a broad-scale spatial structure and high continuity [18]. The value of the variogram at the distance of the range, minus the value of C_0, is considered as the sill (*C*). In the structural analysis, the experimental variogram cannot be directly used and must be replaced by a fitted function called the theoretical variogram. Three of the most commonly used variogram models are the spherical, exponential, and Gaussian models defined as follows:

$$\text{Spherical}: \quad \gamma(h)=\begin{cases} C_0+C\left(\frac{3}{2}\left(\frac{h}{a}\right)-\frac{1}{2}\left(\frac{h}{a}\right)^3\right) & if\ h<a \\ C_0+C & if\ h\geq a \end{cases} \tag{2a}$$

$$\text{Exponential}: \quad \gamma(h)=C_0+C\left(1-\exp\left(\frac{-h}{a}\right)\right) \tag{2b}$$

$$\text{Gaussian}: \quad \gamma(h)=C_0+C\left(1-\exp\left(\frac{-h}{a}\right)^2\right). \tag{2c}$$

For the theoretical variograms that reach their sills asymptotically, like the exponential and Gaussian models, the 'effective range' is defined as the distance at which the variogram value achieves 95% of the sill. The values of the effective range for the exponential and Gaussian models are $3a$ and $\sqrt{3}a$, respectively [19].

The term 'kriging' refers to a variety of geostatistical methods of unbiased estimation based on linear interpolation so that the estimation variance could be minimized. All kriging estimators are variants of the following basic equation [18]:

$$\hat{z}(X)-\mu=\sum_{i=1}^{n}\lambda_i[z_i-\mu(X)] \tag{3}$$

where $\hat{z}$ is the estimated value of an attribute at the point of interest at the location of X; z_i is the observed value at the sampled point; μ is the mean, $\mu(X)$ is the average of samples within the search neighborhood; n represents the number of sample points contributing to the estimation, and; λ_i is the weight assigned to the sample point. The kriging weights are obtained from the solutions of the following n+1 linear simultaneous equations with n+1 unknowns [17]:

$$\begin{cases} \sum_{j=1}^{n}\lambda_j\gamma(X_i-X_j)+\phi=\gamma(X_i-X) & for\ i=1,2,\ldots,n \\ \sum_{j=1}^{n}\lambda_j=1 \end{cases}, \tag{4}$$

where γ is the value of the theoretical variogram, and ϕ is a Lagrange multiplier which ensures that the estimated weights have minimum variance. The weights calculated from the system above are a function of the distance of sample points from one another and from the estimation point.

If the regionalized variable has a known constant mean over the whole domain, the simple kriging is considered; in this case, the parameter $\mu(X)$ in equation (3) is replaced by the stationary mean μ Because such an assumption is often too restrictive, the ordinary kriging is most often used, in which case the mean is considered constant but unknown. If a trend, or drift, exists in the data, the variogram does not stabilize or stabilizes beyond a large distance. In this case, the mean is unknown and non-stationary and the universal kriging model, which incorporates the trend, must be considered [18].

3.2. Variogram fitting

Figure 2 shows directional experimental variograms of the three fracture surfaces along with the corresponding best-fitted models. The direction angle of variogram (β) is measured counter-clockwise from the positive x-axis. The spherical, exponential, and Gaussian models were fitted to the experimental variograms using the weighted least-squares method. The method of weighted nonlinear least squares has been found to be the most robust and reliable method of fitting variogram models [20]. This procedure minimizes the weighted sum of squared residuals (*RSS*) of the experimental variogram data by optimizing different parameters: nugget effect, sill, and range. Each point of the experimental variogram was weighted by $N(h)/\gamma^2(h)$. In such case, greater weights are given to the variogram points with smaller variance (or lower lag distances) and a larger number of pairs [18,20]. The model with the smallest *RSS*

value was automatically chosen as the theoretical variogram.

3.3. Decomposition of spatial variability of surface roughness

As observed in Figure 2, the directional variograms of all the surfaces either do not reach a sill or stabilize over very long distances. This suggests that there is a trend in the topography of the surfaces. The trend needs to be identified before the structural analysis. The trend is typically modeled by a regression surface with the equation of a polynomial of the coordinates, called the base function, as follows [17]:

$$z_t = \sum_{j=0}^{n}\sum_{i=0}^{m} a_{i,j} x^i y^j \tag{5}$$

where z_t is the trend value; $a_{i,j}$ are polynomial coefficients; and m and n are the orders of the polynomial for the x- and y-coordinates, respectively.

The trend surface was initially considered to be planar (i.e., m=n=1). Figure 3a shows a portion of the planar trend surface fitted to the surface S1. To better display the trend in Figure 3, the scale of z-axis was chosen larger than the x- and y-axes scale. The presence of a planar trend means that the fracture surface is not horizontally aligned.

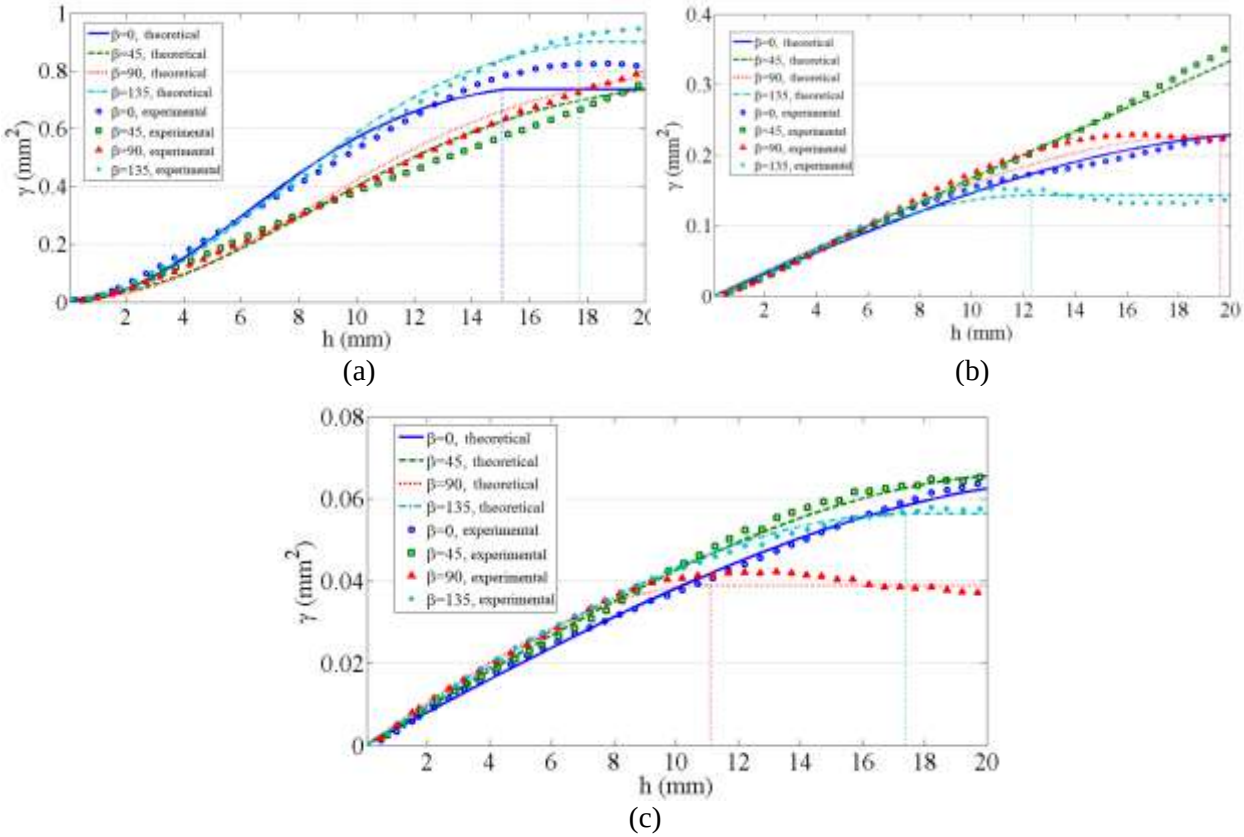

Figure 2. Directional variograms of elevation of the surfaces: S1 (a), S2 (b), and S3 (c)

By subtracting the trend value at each location from the elevation, residual values were computed. Variograms of residuals of S1, S2, and S3 after removing the planar trend are shown in Figure 4. In this case, little changes are observed compared to the variograms of the row data, because the deviations of the measured fracture surfaces from the horizontal are very small.

Since the stationarity conditions were not met by removing the planar trend, polynomial surfaces of higher orders were considered. Figure 3-b shows some parts of a fourth-order surface (m=n=4) fitted to S1. Such polynomial surfaces can represent the large-scale roughness of fracture surfaces, and residuals present the small-scale roughness. In such case, the spatial structure of the fracture surface is described as a polynomial function of order n, and the variogram of residuals (Fig. 5). The trend, which is defined by the base function, is in fact the deterministic component of the spatial variability ($m(X)$), while residual value is a random variable representing the stochastic component of the spatial variability ($e(X)$).

With each increase in the order of the base polynomial, variograms of residuals stabilized at smaller ranges. As observed in Figure 6, no trends exist in the variograms of residuals after removing the fourth-order trend. The smaller the range (i.e., the less the spatial continuity, and the more independent the elevation of nearby points) and the greater the sill (i.e., the

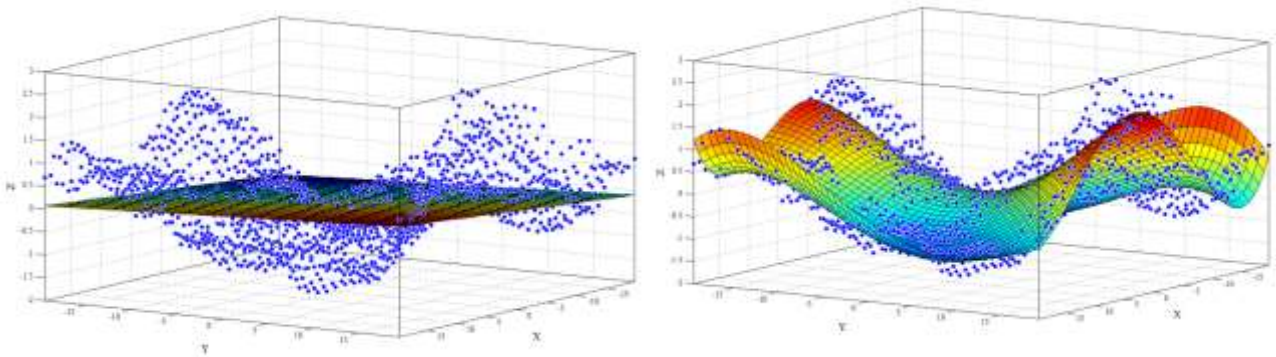

(a) (b)

Figure 3. Part of point cloud of S1 and the fitted polynomial surfaces of order: one (a), and four (b).

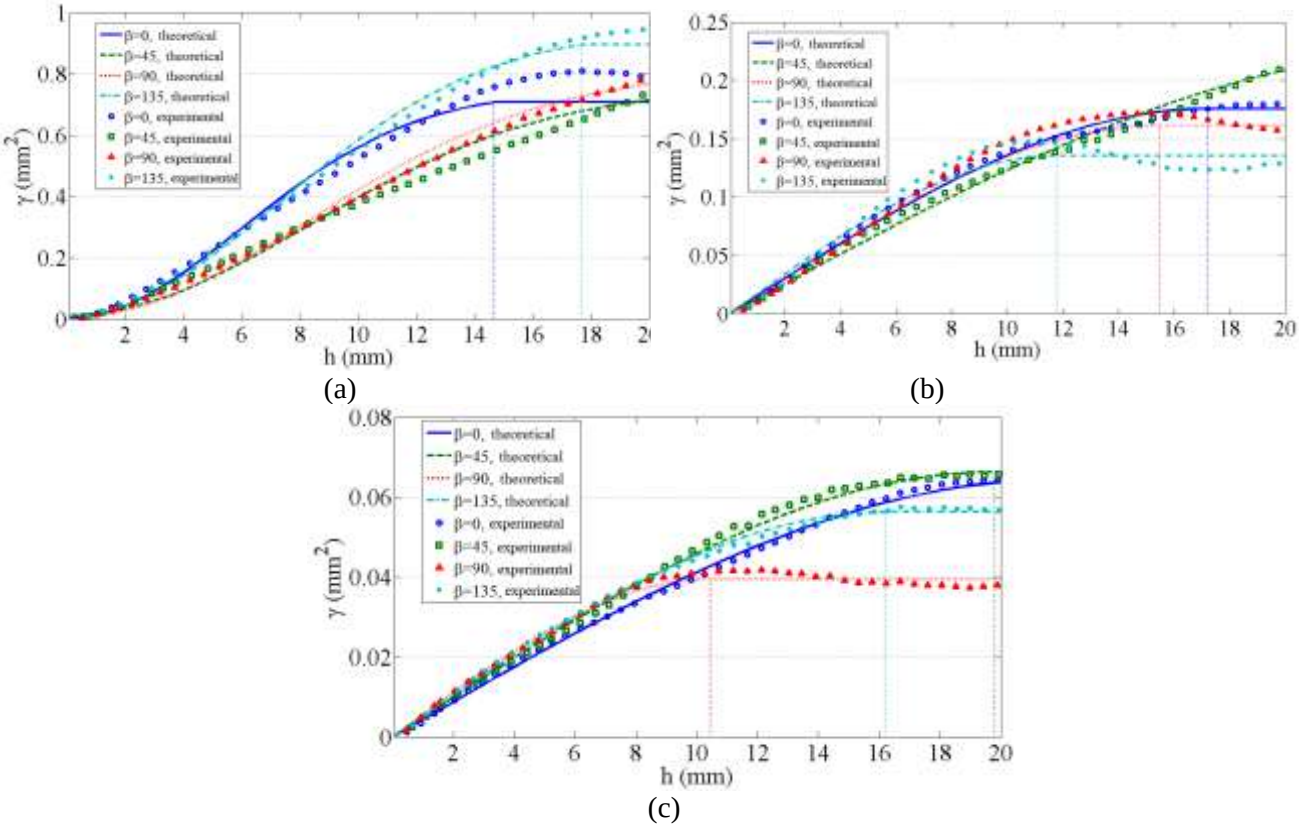

(a) (b)

(c)

Figure 4. Directional variograms of residuals of the surfaces: S1 (a), S2 (b), and S3 (c), after removing the planar trend.

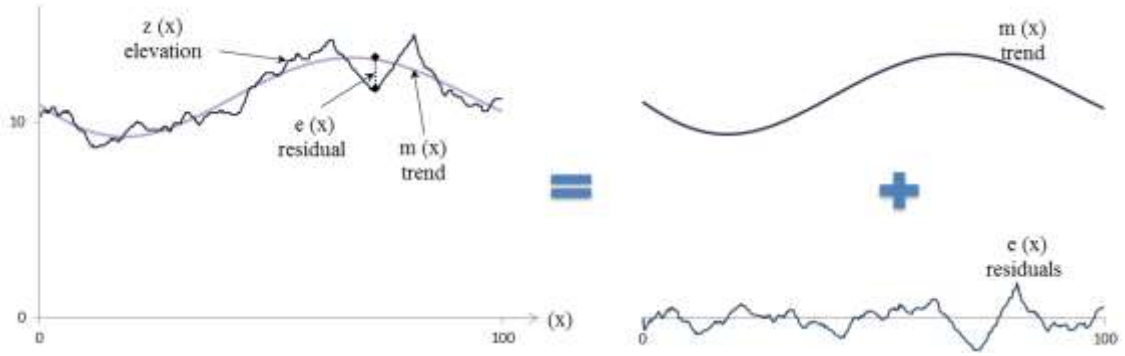

Figure 5. Decomposition of the spatial variation into the deterministic and stochastic components (showed for the standard profile No. 9 of roughness).

higher the variability), the rougher the rock fracture surface. Figure 7 shows the values of the range and peak (C_0+C) of omnidirectional variograms of the fracture surfaces versus the order of the base polynomial increased up to five. In order to indicate changes of the range and peak together on one graph, they were normalized by their maximum values. With increasing the order of the base function, the peak value of variograms decreased as well in a way similar to the range decrease. In the following analyses, the fourth-order polynomial was considered as the base function. Values of the variograms range lie within the scale of surface asperities (micro-roughness) of rock fractures which mainly control the mobilization of the shear strength.

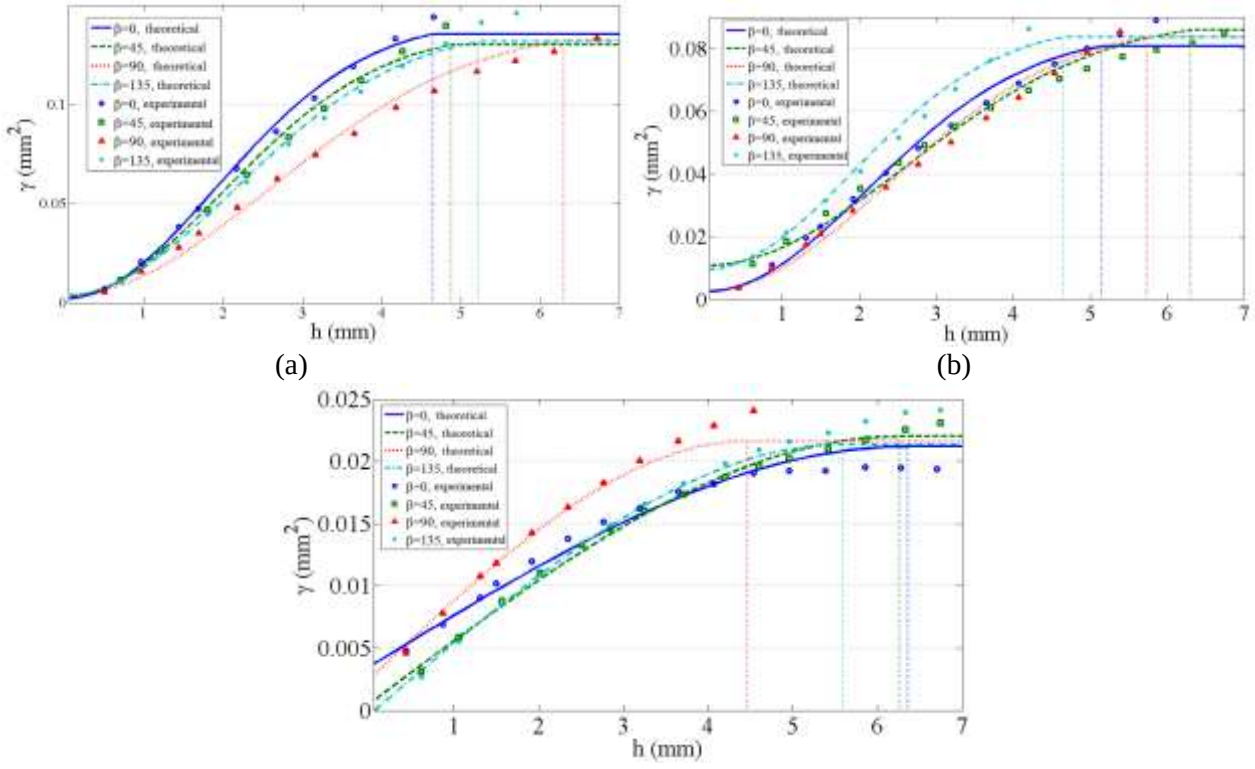

Figure 6. Directional variograms of residuals of the surfaces: S1 (a), S2 (b), and S3 (c), after removing the fourth-order trend.

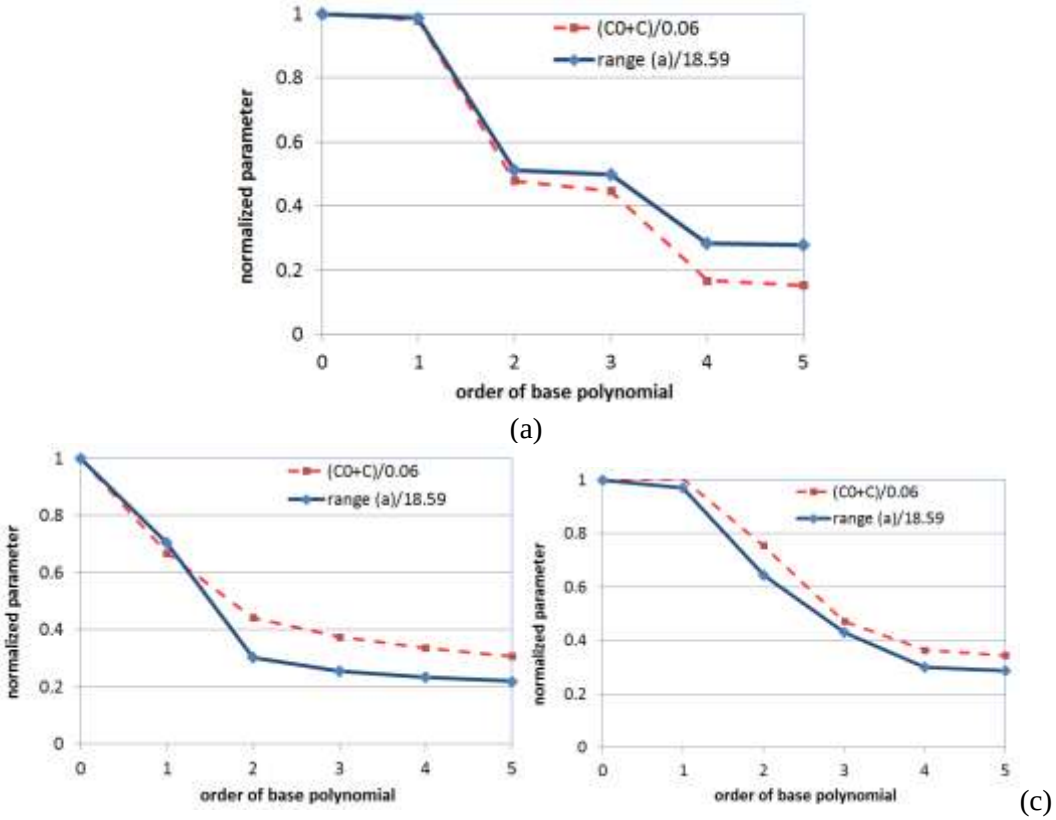

Figure 7. Normalized values of the range and peak of omnidirectional variogram of the surfaces: S1 (a), S2 (b), and S3 (c) versus the order of base polynomials.

3.4. Roughness anisotropy

As observed in Figure 6, the variograms of each surface have different ranges and nearly the same sills in different directions after removing the trend. This is typical of the geometric anisotropy of the fracture roughness which can be modeled by the ellipse of ranges. Figure 8 shows the anisotropy ellipses fitted to ranges of the variograms of the residuals. An anisotropy ellipse is characterized by three parameters: maximum range (a_{max}), the direction of maximum continuity (α) measured counter-clockwise from the positive x-axis, and the anisotropy ratio (R_{ani}) defined as the ratio of the maximum range to the minimum. Residuals of the three surfaces have almost identical R_{ani} and a_{max} values, but different values of α, C, and/or model types.

3.5. Regression-kriging estimation

In this section, the regression-kriging (RK) method is employed for interpolating the topography of rock fracture surfaces. The RK method is a spatial interpolation technique that combines a regression of the regionalized variable with kriging of the residuals. It is similar to a universal kriging method in which a regression function of coordinates is considered as the trend. In this method, trend values at desired locations obtained from the regression function (a fourth-order polynomial, in here) are added to the values of kriged residuals in order to provide an estimate of the elevation. The leave-one-out cross-validation (LOOCV) technique was used to evaluate the performance of the RK method. In each iteration of the LOOCV procedure, one of the measured points is left out temporarily, and its elevation is estimated using the neighboring points [21]. The LOOCV error was calculated as the root mean square of the differences between the estimated values of elevation and the real elevation values. The cross-validation of the RK method was carried out over a grid with a size of 1 mm for the three measured topographies. The directional variograms (Fig. 8) and elliptical search neighborhoods equal to 2/3 of the range ellipses of each surface were

used in the kriging estimation of residuals. The calculated root mean square error (*RMSE*) of the RK estimation was 0.14, 0.11, and 0.06 mm for the surfaces S1, S2, and S3, respectively (Fig. 9). Figure 10 shows a real profile from each surface along with the corresponding profile reconstructed by the above-mentioned procedure. The application of kriging was resulted in smoothing of the roughness profiles. As a result, the efficiency of the RK method was improved with decreasing the surface roughness.

4. Detection of damaged zones

In order to study the spatial structure of damaged areas, it is required to identify their locations. Two approaches can be found in the previous studies for detecting damaged zones, both of which are based on considering a threshold. The first approach is comparing the 3D topography of the initial and sheared fracture surfaces and detecting the damaged zones as the points having a height reduction greater than a specified threshold [7,14]. In this method, the fracture surface before and after shearing needs to be scanned. selection of an appropriate threshold is a challenging stage. The second approach is to detect the damaged zones by image-processing of the sheared surface photograph in which the intact and degraded zones have different colors [13]. In this method, there is no need for scanning the fracture surface after the shear test. Moreover, this approach provides a visual comparison which ensures whether the value of the segmentation threshold is properly chosen.

In this study, an image-processing technique was employed to locate the damaged zones on the topography of the fracture surfaces before/after shearing. First, the painted surfaces were digitally photographed

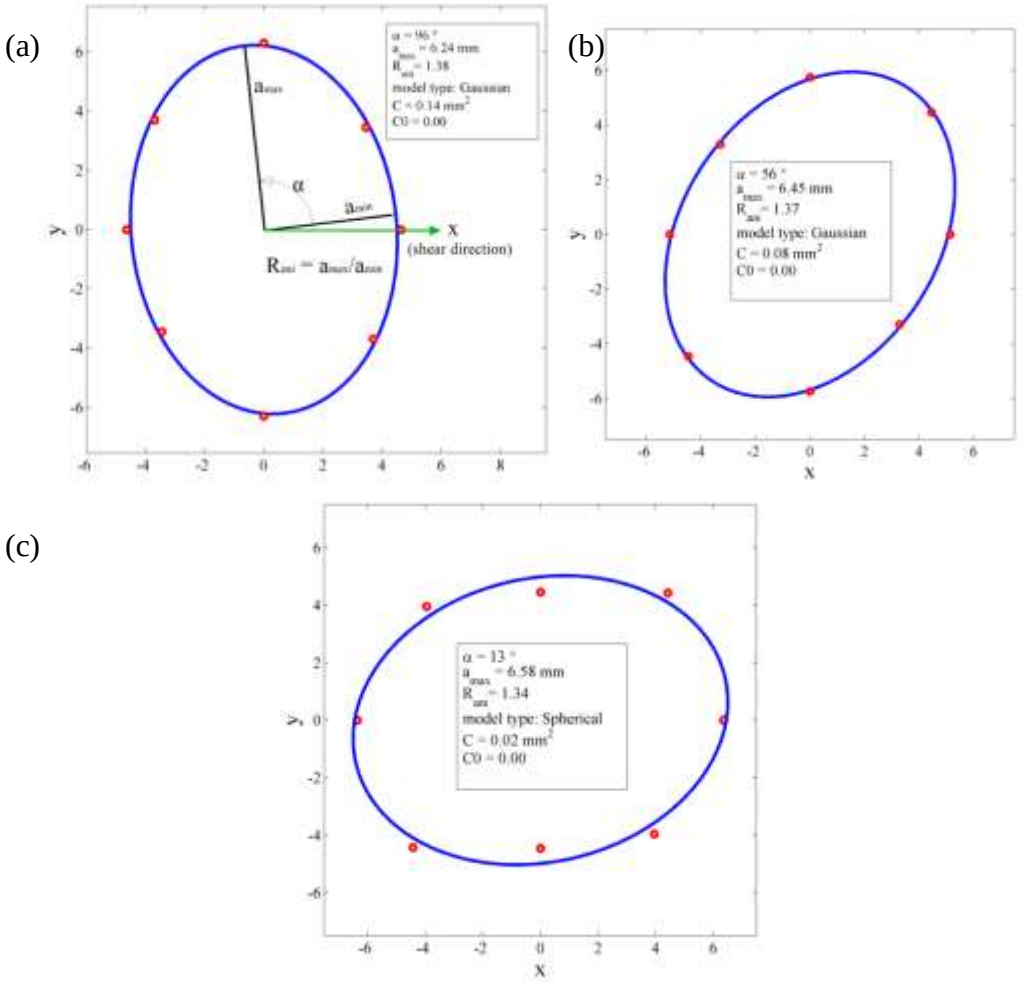

Figure 8. Anisotropy ellipses for variograms of residuals of the surfaces: S1 (a), S2 (b), and S3 (c).

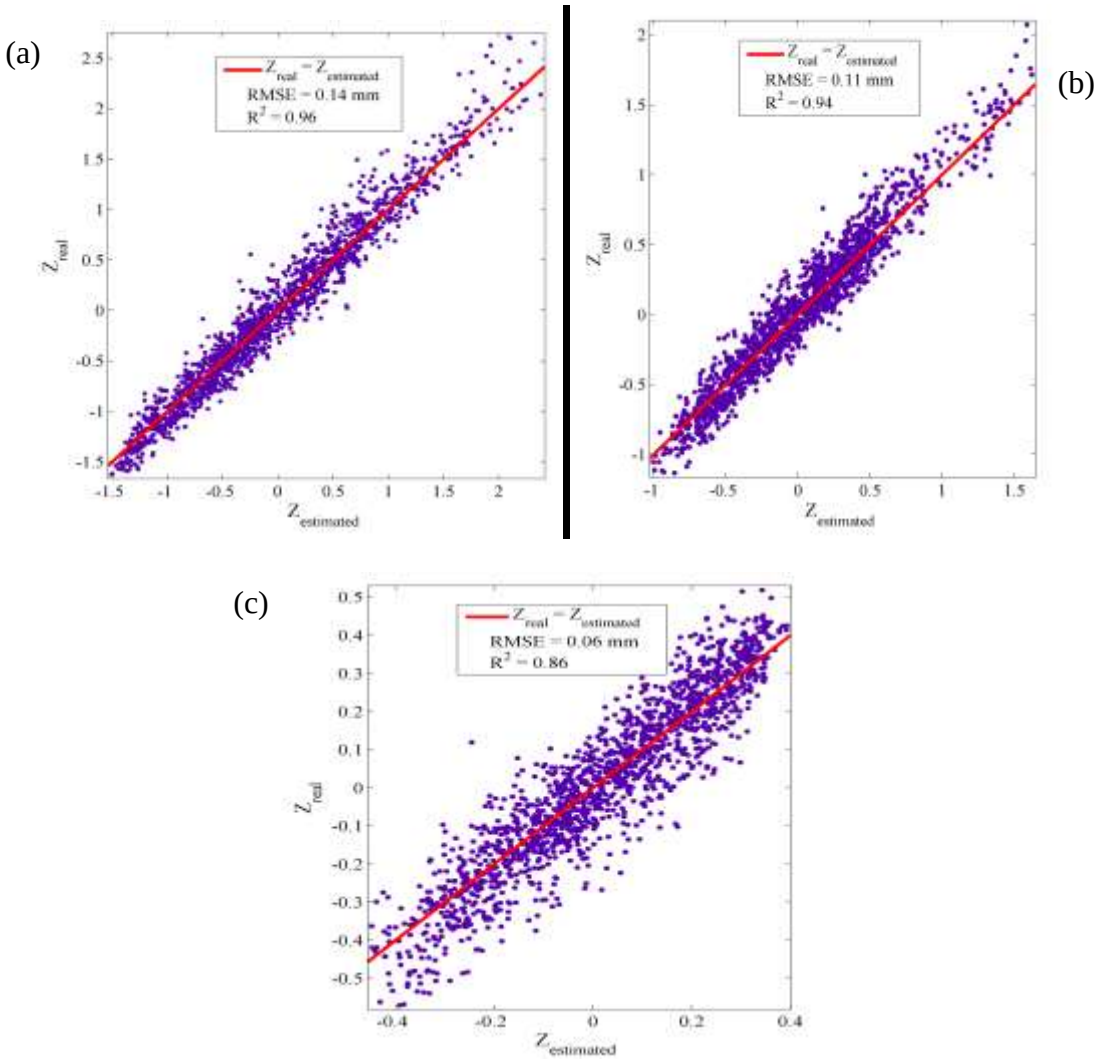

Figure 9. Cross validation plots for RK interpolation of the surfaces: S1 (a), S2 (b), and S3 (c)

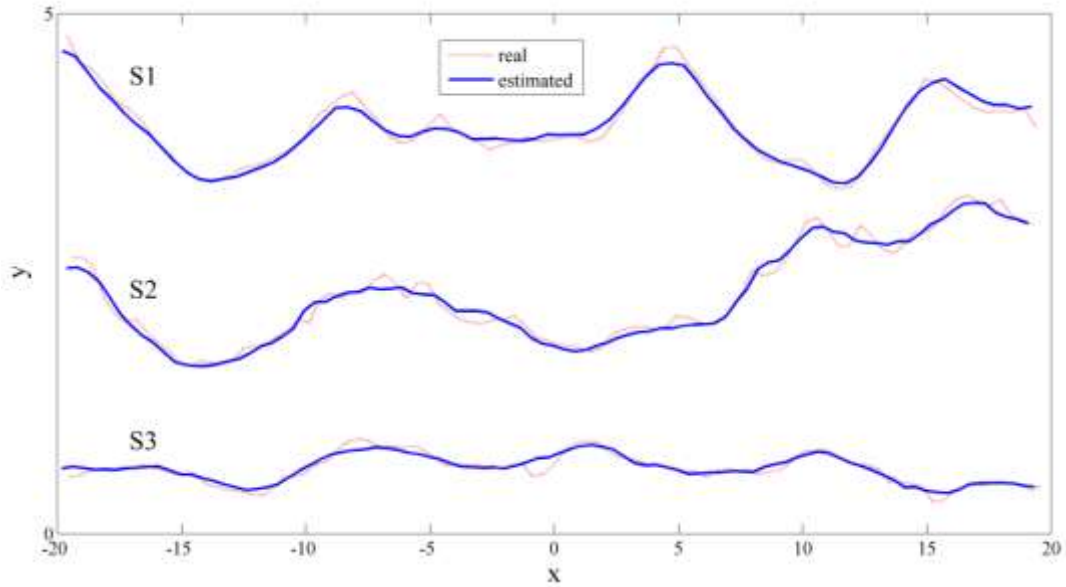

Figure 10. Profiles reconstructed by the RK method along with the corresponding real profiles.

after shearing such that the optical axis was parallel to the *z*-axis (the camera lens parallel to the *xy*-plane). Figure 11a shows the image of the surface S1 after shearing in which the light color represents the damaged areas. By comparing pixel values in the corresponding gray-level image with a threshold value, a binary (black and white) image is obtained in which degraded zones having white pixels are completely separated from black intact areas (Fig. 11b). This process is known as the threshold-based segmentation of the image [22]. An image-processing code was written in MATLAB to perform the segmentation of the sheared surface image. The choice of the appropriate threshold value depends on the color intensity of the intact and degraded areas. Filters and morphological operators can be applied to the binary image for removing noises and tiny artifacts. The parameter of a_s can be calculated as the ratio of the number of white pixels to the total number of pixels (blacks and whites) of the fracture surface in the binary image. The estimated values of a_s were 7.5%, 18%, and 7% for S1, S2, and S3, respectively. Each connected component of white pixels was then considered as one damaged zone. Figure 11-c indicates the zoning map of the damaged areas of S1. For the studied surfaces, 46, 263, and 34 zones of degradation were respectively detected (in total, 343 zones) with different sizes and shapes. As can be seen, a damaged zone may not be fully filled with white pixels, and an island of intact areas may exist within it.

Now, the 2D binary image containing information of the location of the damaged zone must be superimposed onto the 3D topography of the fracture surface. To do this, both grids of the topography and image pixels need to have the same size. The diameter of the fracture surface comprises 2205 pixels on the digital image, taken by a compact camera with a resolution of 7.5 megapixels. As a result, pixel size is equal to 60/2205=0.027 mm that is smaller than the grid size of the 3D measurement (i.e., 0.05 mm). Therefore, image dimensions need to be decreased 0.027/0.05=1.85 times so that both the grids are of the same size. The superposition of the 2D binary image and the initial topography of the fracture surfaces is shown in Figure 12. In this case, *x*- and *y*-coordinates of all the damaged zones are determined, and the corresponding *z*-coordinate can be obtained using elevation data of the surface topography before or after shearing, depending on which one is intended.

5. Spatial structure in damaged zones

Prior to investigating the spatial structure of damaged zones, the global trend of sheared surfaces was examined, and polynomials of different orders were again fitted over the fracture surfaces after shearing. Comparing the trend surfaces before and after shearing showed almost no difference. This demonstrates that the surface degradation occured within small-scale asperities not over large-scale undulations.

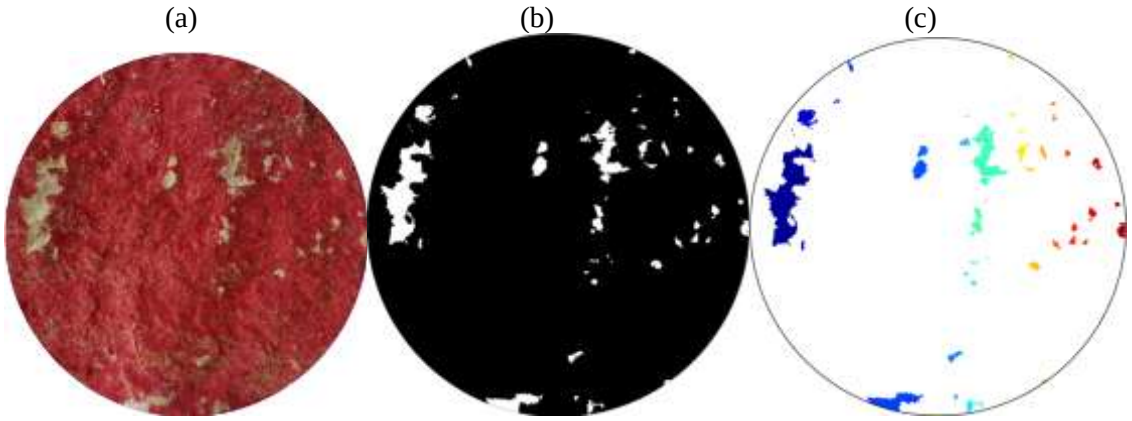

Figure 11. Original image of the sheared S1 (a), binary image obtained from segmentation (b), and zoning map of damaged areas (c).

5.1. Variography of damaged zones before shearing

In order to understand the evolution of spatial structure with shearing, zonal variograms of residuals before the shear test need to be calculated at the locations corresponding to the damaged zones. Due to the heterogeneity of the surface roughness, the zonal variograms are not necessarily identical and can be different in range, sill, and anisotropy properties (Figure 12). The issue of modeling the zonal variograms suggests that many of the damaged zones are so small that their variograms cannot be plotted up to a sufficiently large distance. Therefore, the concept of 'pseudo-zonal variogram' is introduced and used in the followings. The value of the pseudo-zonal variogram at a given h, is defined as the average of the term $[z(X+h)-z(X)]^2$ calculated for every damaged zone with a size greater than $2h$. Thus, the pseudo-zonal variogram of a fracture surface before/after shearing is formulated as below:

$$\gamma(h)=\frac{1}{2\sum_{j=1}^{M}N_j(h)}\sum_{j=1}^{M}\sum_{i=1}^{N_j(h)}[z(X+h)-z(X)]^2, \quad (6)$$

where M is the number of damaged zones; and $N_j(h)$ is the number of pairs of points with a distance of h in the j-th zone. The overall spatial structure of discrete target zones distributed in a global surface can be characterized. The pseudo-zonal variograms can be also calculated in different directions. Ellipses of the directional global, pseudo-zonal, and zonal variograms of the residuals prior to the shear test are shown in Figure 13. The global variogram has a higher range and lower sill, compared with the pre-shearing pseudo-zonal and zonal variograms. This means that the damaged zones have an initial roughness greater than the average roughness of the surface.

5.2. Evolution of spatial structure with shearing

Figure 14 shows the three pseudo-zonal variograms and several zonal variograms of damaged zones before and after shearing. The spatial continuity at the damaged zones has increased due to asperity degradation. It is observed that the increase of variogram range is greater in the shear direction (x-axis) such that the direction of maximum continuity leans toward the shear direction. Therefore, if the range ellipse of a damaged zone was initially elongated toward the shear direction, the anisotropy would increase with shearing (for

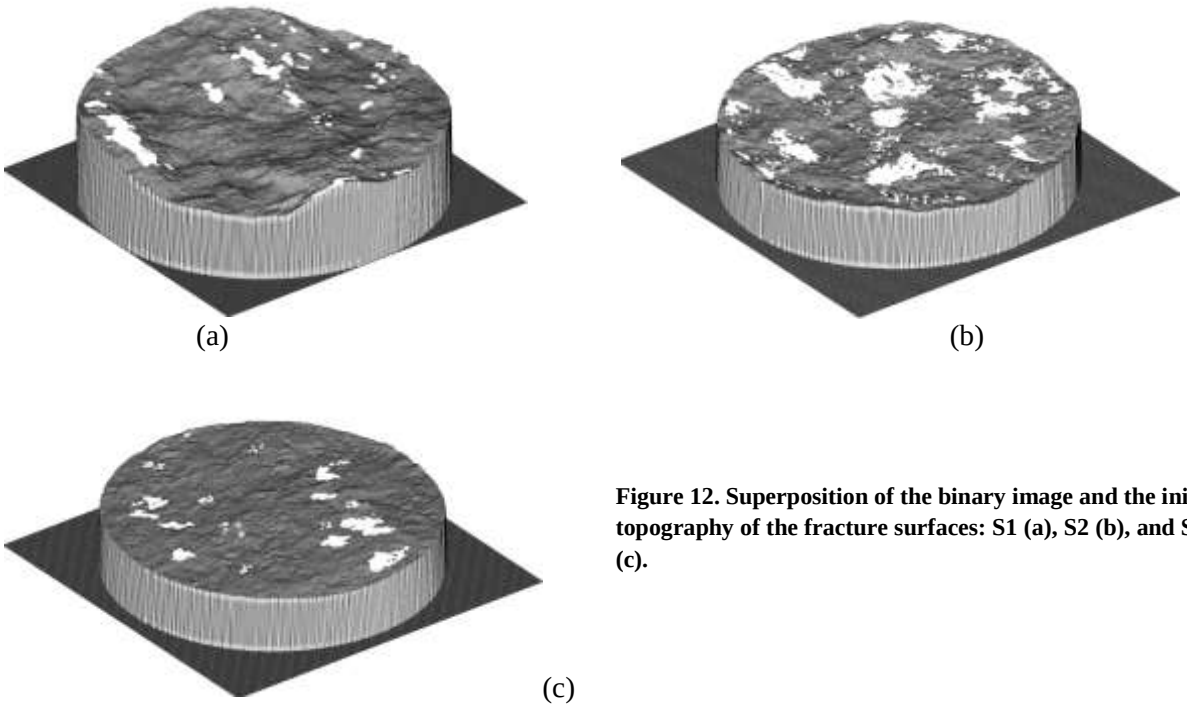

(a) (b)

(c)

Figure 12. Superposition of the binary image and the initial topography of the fracture surfaces: S1 (a), S2 (b), and S3 (c).

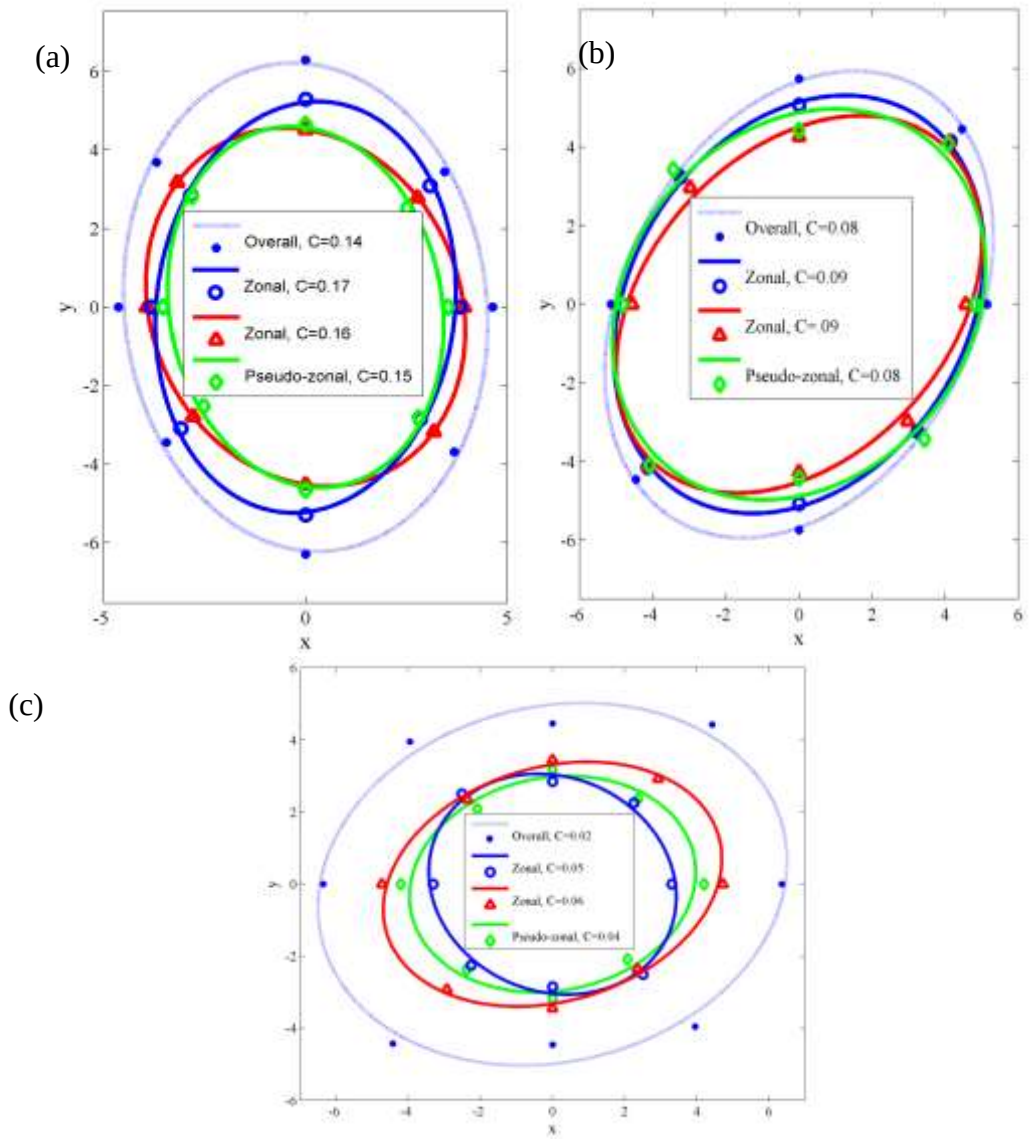

Figure 13. Ellipses of the directional global, pseudo-zonal, and zonal variograms of residuals of: S1 (a), S2 (b), and S3 (c), before shearing.

example, in Fig. 14-g), and if the minor semi-axis of continuity was originally oriented along the shear direction, the anisotropy would decrease (for example, in Fig. 14-a). The sill of the variograms of damaged zones indicates only a slight reduction with asperity degradation. This reveals that the roughness reduction caused by shearing was mainly reflected as increasing the spatial continuity, instead of decreasing the variability.

5.3. Kriging of degraded zones

The RK method was used to reconstruct the topography of areas degraded by shearing. For the damaged zones having a sufficient breadth (4, 13, and 4 zones in S1, S2, and S3, respectively), their directional zonal variograms after shearing were used for kriging the residuals, and the directional pseudo-zonal variogram of each surface was considered for its small zones. The kriged residuals at the damaged zones were then added to the value of the global trend surface to provide an estimate elevation. It is worth noting that for kriging the residual value at a location falling in a given damaged zone, only the neighboring sample points were considered that belonged to the same zone. The LOOCV

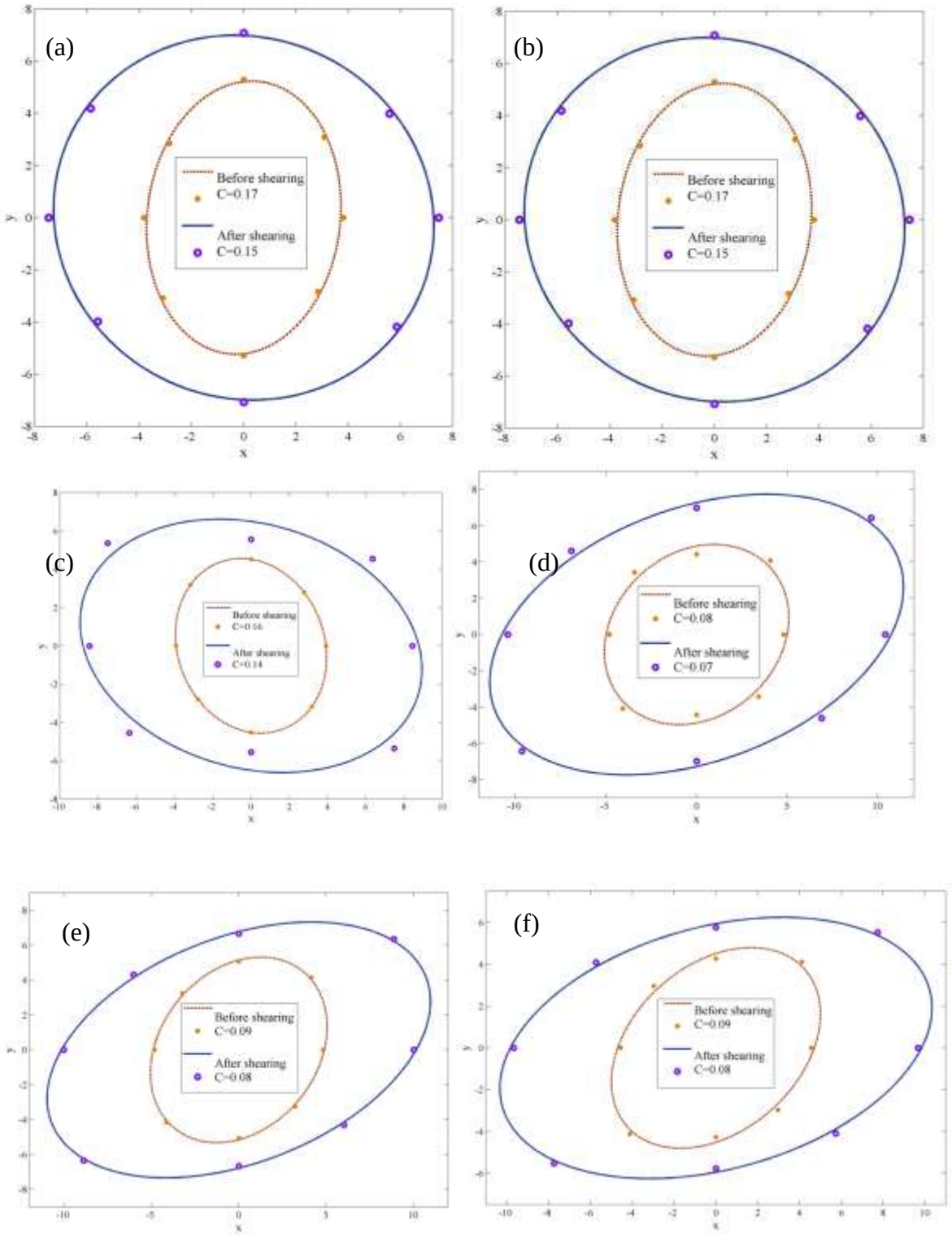
(a)
Before shearing
C=0.17
After shearing
C=0.15
(b)
Before shearing
C=0.17
After shearing
C=0.15
(c)
(d)
Before shearing
C=0.08
After shearing
C=0.07
(e)
Before shearing
C=0.09
After shearing
C=0.08
(f)
Before shearing
C=0.09
After shearing
C=0.08

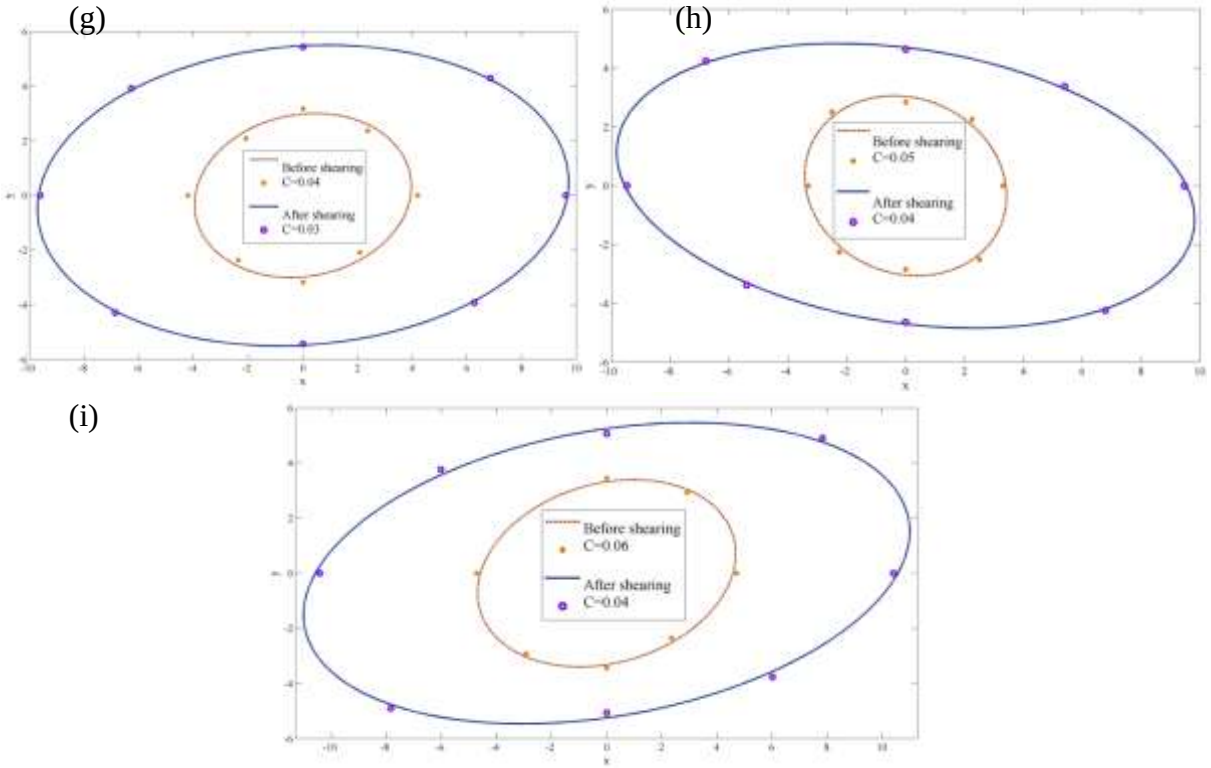

Figure 14. Comparison of variograms of damaged zones before and after shearing: the pseudo-zonal variogram ellipse for S1 (a), two zonal variogram ellipses for S1 (b, c), the pseudo-zonal variogram ellipse for S2 (d), two zonal variogram ellipses for S2 (e, f), the pseudo-zonal variogram ellipse for S3 (g), and two zonal variogram ellipses for S3 (h, i).

method was again used to comprehensively evaluate the spatial estimation in each degraded zone, considering a grid size of 1 mm. The calculated values of *RMSE* were respectively 0.08, 0.07, and 0.05 mm for interpolating the damaged zones of S1, S2, and S3 which are smaller than the *RMSE* values of the pre-shear surface interpolations. One reason for this accuracy increase is that the asperity degradation results in smoothing of the geometry at damaged areas of the surface, and makes them better suited for being kriged. Application of the zonal/pseudo-zonal variograms instead of using the global variogram is in turn another reason for increasing the accuracy of interpolation of damaged areas compared to the whole initial surface.

6. Conclusions

The variogram analysis of fracture surface allows the full 3D description of the roughness instead of summarizing it into a single roughness parameter. The variography of the surfaces suggested that they have a notable non-linear trend in their geometries and are not stationary. After eliminating fitted polynomial trends, residuals indicated further stationarity with increasing the polynomial order up to five. Both the sill and range of variograms decreased with removing the non-linear trend. In fact, the spatial structure of rock fracture surfaces can be decomposed to one deterministic component characterized by a base polynomial function and representing large-scale undulations, and one stochastic component described by the variogram of residuals and representing the small-scale roughness. The decomposition of the spatial structure of rock fracture surfaces with such an approach, which has not been formerly addressed, is absolutely necessary from both the geostatistical and mechanical point of view.

In total, 343 zones of degradation in a variety of sizes, shapes, initial roughness characteristics, local stress fields, and asperity strength values were identified and analyzed. Since many of the damaged zones were so small, only a limited number of zonal

variograms could be modeled in practice. In order to characterize the overall spatial structure of the damaged zones, the concept of pseudo-zonal variogram was proposed which takes the information of every damaged zone into account.

The comparison of the trend surfaces before and after shearing did not show any difference. This indicates that the surface degradation has occurred within small-scale asperities. The results show that the spatial continuity at the damage location increases due to asperity degradation. The increase of variogram range is anisotropic and tends to be higher in the shear direction; as a result, the direction of maximum continuity rotates towards the shear direction. Therefore, the anisotropy in damage locations may increase or decrease with shearing, depending on how the range ellipse was initially oriented relative to the shear direction. The sills of variograms of damaged zones indicate only a slight reduction with asperity degradation. This demonstrates that the roughness reduction due to shearing is mainly reflected as increasing the spatial continuity, instead of decreasing the variability.

Finally, the regression-kriging method was used to interpolate the morphology of the intact surfaces and degraded areas. The geometry of the fracture surface reconstructed by this method was found to be smoothed compared with the real geometry. The interpolation error for the damaged zones was smaller than for the intact surface. One reason for this increase in the accuracy is that the asperity degradation results in smoothing of the geometry at degraded areas of the surface, and makes them better suited for being kriged. On the other hand, application of the zonal and pseudo-zonal variograms instead of using the global variogram is in turn another reason for increasing the accuracy of interpolation of damaged areas compared to the whole initial surface.

The modeling of the evolution of the variogram of fracture surface with shearing can be considered as the subject of future work. As such, a methodology may be established to predict the 3D geometry of the sheared surface after the direct shear test.

References

[1]. Barton, N., Choubey, V. (1977). The shear strength of rock joints in theory and practice. Rock Mechanics:10, p.1–54.

[2]. Tse, R., Cruden, D.M. (1979). Estimating joint roughness coefficients. International Journal of Rock Mechanics & Mining Sciences & Geomechanics Abstracts: 16, p.303–7.

[3]. Ge, Y., Kulatilake, P.H.S.W., Tang, H., Xiong, C. (2014). Investigation of natural rock joint roughness. Computers and Geotechnics: 55, p.290–305.

[4]. Huang, S.L., Oelfke, S.M., Speck, R.C. (1992). Applicability of fractal characterization and modelling to rock joint profiles. International Journal of Rock Mechanics & Mining Sciences & Geomechanics Abstracts: 29, p.89–98.

[5]. Marache, A., Riss, J., Gentier, S., Chiles, J.P. (2002). Characterization and reconstruction of a rock fracture surface by geostatistics. International Journal for Numerical and Analytical Methods in Geomechanics: 26, p.873–896.

[6]. Hirotaka, S., Grasselli, G. (2010). Geostatistical downscaling of fracture surface topography accounting for local roughness. Acta Geotechnica: 5, p.127–138.

[7]. Grasselli, G., Wirth, J., Egger, P. (2002). Quantitative three-dimensional description of rough surface and parameter evolution with shearing. International Journal of Rock Mechanics & Mining Sciences: 39, p.789–800.

[8]. Brown, E.T. (Ed). (1981). ISRM suggested methods: rock characterization, testing and monitoring. Pergamon Press, Oxford.

[9]. Ladanyi, B., Archambault, G. (1970). Simulation of the shear behaviour of a jointed rock mass. In: Proceedings of the 11th Symposium on Rock Mechanics: Theory and Practice, Berkeley, p.105–125.

[10]. Kwafniewski, M.A., Wang, J.A. (1997). Surface roughness evolution and mechanical behavior of rock joints under shear. International Journal of Rock Mechanics & Mining Sciences: 34, 157.e1–157.e14.

[11]. Asadi, M.S., Rasouli, V., Barla, G. (2012). A Bonded Particle Model Simulation of Shear Strength and for Rough Rock

Fractures. Rock Mechanics and Rock Engineering: 45, p.649–675.

[12]. Homand, F., Belem, T., Souley, M. (2001). Friction and degradation of rock joint surfaces under shear loads. International Journal for Numerical and Analytical Methods in Geomechanics: 25, p.973–999.

[13]. Genteir, S., Riss, J., Archambault, R., Flamand, R., Hopkins, D. (2000). Influence of fracture geometry on the shear behavior. International Journal of Rock Mechanics & Mining Sciences: 37, p.161–174.

[14]. Grasselli, G. (2001). Shear strength of rock joints based on quantified surface description. Doctoral Thesis. Swiss Institute of Technology (EPFL).

[15]. Amiri Hossaini, K., Babanouri, N., Karimi Nasab, S. (2014). The influence of asperity deformability on the mechanical behavior of rock joints. International Journal of Rock Mechanics & Mining Sciences: 70, p.154–161.
(doi: 10.1016/j.ijrmms.2014.04.009)

[16]. Bergmann, D., Galanulis, K., Winter, D. (1997). Advanced 3d fringe projection system. GOM mbH, Braunschweig.

[17]. Goovaerts, P. (1997). Geostatistics for natural resources evaluation. Oxford University Press, New York.

[18]. Journel, A.G., Huijbregts, C.J. (1978). Mining Geostatistics. Academic Press, London.

[19]. Deutsch, C. V., Journel, A. G. (1998). GSLIB Geostatistical Software Library and User's Guide, second ed. Oxford University Press, New York.

[20]. Cressie, N. (1985). Fitting variogram models by weighted least squares. Mathematical Geology: 17, p.239–252.

[21]. Tomczak, M., (1998). Spatial interpolation and its uncertainty using automated anisotropic inverse distance weighting (IDW)—crossvalidation/jackknife approach. Journal of Geographic Information and Decision Analysis: 2, p.18–30.

[22]. Gonzalez, R.C., Woods, R.E. (2002). Digital Image Processing. Prentice Hall.